ROYAL SOCIETY
OF CHEMISTRY

PAPER

Check for updates

Strategic Ni-doping improved electrocatalytic H$_2$ production by Bi$_3$O$_4$Br in alkaline water†

Manodip Pal,[a] Rathindranath Biswas, [ID][a] Sanmitra Barman*[b] and Arnab Dutta [ID] *[acd]

Establishing a cost-effective and efficient electrocatalytic pathway for the hydrogen evolution reaction (HER) is the key to our quest for a carbon-neutral energy landscape. We report a simple and straightforward approach to synthesize an efficient, stable, and low-cost noble metal-free Bi$_3$O$_4$Br electrocatalyst. Tactical doping of Ni ions into Bi$_3$O$_4$Br effectively enhanced the conductivity, accelerated the charge transfer process, and provided more catalytic active sites to significantly boost the alkaline electrochemical HER performance of Bi$_3$O$_4$Br. This Ni-doped Bi$_3$O$_4$Br exhibited a lower overpotential of 662 mV compared to that of Bi$_3$O$_4$Br (736 mV) at a higher current density (50 mA cm^{-2}). Additionally, the HER kinetics were also enhanced in terms of Tafel slope for this doped material (159 mV dec^{-1}) compared to the pristine Bi$_3$O$_4$Br (245 mV dec^{-1}), which coincides with a significant improvement in the mass activity (52 A g^{-1} to 98 A g^{-1}). Notably, the overpotential of Ni-doped Bi$_3$O$_4$Br was further reduced to 614 mV at the same current density of 50 mA cm^{-2} during photoelectrochemical HER performance testing, and the faradaic efficiency was improved from 79% to 87%. Finally, an enhanced durability of the material was observed for Bi$_3$O$_4$Br following the Ni-doping. Hence, this strategy highlights the importance of unravelling upgraded catalytic behaviour for abundant materials with rational doping.

Introduction

Hydrogen is a popular choice of future energy material for transducing renewable energy to practically usable electricity with minimal greenhouse gas emissions.[1–4] In this flow of events, the hydrogen evolution reaction (HER) from abundant water is reckoned as a key step. Water electrolysis is looked upon as the primary pathway for industrial-scale HER, which is required to be executed at a rapid rate with low overpotential requirements. Over the last few decades, extensive research efforts have been made to develop an electrocatalyst that can produce hydrogen *via* the electrocatalytic splitting of water at a lower overpotential with appreciable rates.[5–9] Electrocatalytic water splitting can be carried out in both acidic and alkaline media, and the lack of acid-tolerant counter electrode materials is a bottleneck for the production of multimillion tons of H$_2$ *via* acidic electrolyzers.[10–12] Therefore, major emphasis has been

given to the quest for a stable and highly active catalyst for alkaline HER in the past few decades.[7,13] Moreover, similar efforts are being made to develop compatible, stable, and efficient electrocatalysts for the other half-cell reaction of water electrolysis: the complementary oxygen evolution reaction (OER) under similar conditions. The appropriate assembly of HER and OER electrocatalysts is vital for a fully functional alkaline water electrolyzer.[14–19] Here, the challenge is to generate an electrocatalyst composed of earth-abundant elements that can display good stability and high efficiency while executing the HER in an alkaline medium.[20–22] There has been a plethora of electrocatalysts containing earth-abundant transition metals developed recently for electrocatalytic water splitting.[23–25]

Bismuth oxyhalides (BiOX, where X = Cl, Br or I), classified as a ternary compound, have a layered structure consisting of repetitive units of [Bi$_2$O$_2$]$^{2+}$ and X$^-$, which are typically held together by van der Waals forces of attraction. These materials have emerged as a serious contender for practical electrocatalytic applications owing to their ease of preparation, excellent photocatalytic properties, relative nontoxicity, and low cost. These materials are promising photocatalysts due to their inherent wide bandgap that broadens their absorption profile through the ultra-violet and visible region. Nevertheless, these materials exhibit facile charge recombination, leading to low catalytic responses in the absence of any charge-trapping centers.[26,27] Tactical incorporation of surface defects in these nanomaterials is reckoned as a key approach for stabilizing the charge-separated holes and electrons, which in turn proceeds

[a] Chemistry Department, Indian Institute of Technology Bombay, Powai, Maharashtra 400076, India. E-mail: arnab.dutta@iitb.ac.in

[b] Center for Advanced Materials and Devices (CAMD), BML Munjal University, Haryana-122413, India. E-mail: sanmitra.barman@bmu.edu.in

[c] National Center of Excellence, CCU, Indian Institute of Technology Bombay, Powai, Maharashtra 400076, India

[d] Interdisciplinary Program in Climate Studies, Indian Institute of Technology Bombay, Powai, Maharashtra 400076, India

to effective catalysis. Enriching the bismuth oxyhalide framework with additional bismuth ions is found to produce promising results.[28] These bismuth-rich bismuth oxyhalides are formulated as $Bi_mO_nX_p$, where X = Cl, Br or I, and m, n, and p are various stoichiometric proportions.

Among these bismuth-rich bismuth oxyhalides, Bi_3O_4Br is one of the popular choices due to the ease of synthesis, tuneable morphology with controllable stoichiometry, and enhanced visible light absorption properties.[29–31] It is reported that Bi_3O_4Br has a layer structure composed of $[Bi_3O_4]^{1+}$ units attached to the Br^- by van der Waals force of attraction. Two bismuth coordination environments were reported for this material. In the first coordination geometry, the bismuth ion is ligated to three oxygen atoms and one bromine atom. In the second environment, one bismuth atom is attached to four oxygen atoms in the unit cell of Bi_3O_4Br. To further tailor the catalytic properties of Bi_3O_4Br, the bismuth is substituted with a transition metal, such as Co, which was reported to be an effective strategy. Recently, single atom (Co)-doped Bi_3O_4Br was also reported that illustrated remarkable photo-electrocatalytic activity for carbon dioxide conversion.[29] Jiang et al. developed Ag-doped Bi_3O_4Br for the efficient photodegradation of bisphenol-A.[32] Wang et al. fabricated an Ni-doped $CsPbBr_3/Bi_3O_4Br$ heterostructured material for efficient photocatalytic CO_2 conversion following a Z-scheme of electron transfer.[33] Hence, Bi_3O_4Br-based materials have been widely used in the field of photochemical applications.

In this work, we have synthesized a Ni-doped (0.4 atomic %) Bi_3O_4Br material and probed its reactivity as an electrocatalyst in an alkaline aqueous medium (pH ∼14.0). The inclusion of Ni 3d-bands into the Bi 4f orbitals reduced the original bandgap of the Bi_3O_4Br, which was supported by the X-ray photoelectron spectroscopy (XPS) data. During the assembly of the electrocatalytic material, polyvinylpyrrolidone (PVP) was added to prevent any lateral growth of Bi_3O_4Br nanocrystals. The PVP directly interacts with Bi_3O_4Br, as a passivation layer is created around the crystal core through the strong interaction between the Bi^{3+} and the oxygen and nitrogen atoms present on the pyrrolidone ring, resulting in the formation of 2D-plate-shaped nanocrystals. The catalyst is fully characterized by an array of analytical techniques, such as XRD, XPS, UV-vis, FTIR, and Raman spectroscopy. For comparison, we have also synthesized pristine Bi_3O_4Br by following the same protocol and compared its electrocatalytic HER properties with those of the Ni-doped Bi_3O_4Br in an aqueous alkaline (1.0 M KOH, pH 14.0) medium.

Experimental procedures

Reagents and materials

All the chemicals mentioned are of analytical grade unless otherwise mentioned, which were used as procured without further purification. $Bi(NO_3)_3·5H_2O$ (98%), KCl, KBr, HNO_3 (70%), $Ni(\text{II})(CH_3COO)_2·4H_2O$ (98%), polyvinyl pyrrolidone (PVP), mannitol, ethanol (absolute), and NaOH (>97%) were purchased from Sigma Aldrich, India. Milli Q water (resistivity 18.2 MΩ cm) was used throughout for all the experiments. The pH value was maintained by using buffer capsules (Merck, India).

Synthesis of Bi_3O_4Br and Ni-doped Bi_3O_4Br

Bi_3O_4Br and Ni-doped Bi_3O_4Br nanoparticles were prepared by the hydrothermal method under similar experimental conditions as reported in the literature.[29] In summary, 0.5 mmol of $Bi(NO_3)_3·5H_2O$ was added to 0.2 g polyvinyl pyrrolidone (PVP) and 0.1 M mannitol solution in 15.0 mL of Millipore water. 0.005 mmol of $Ni(\text{II})(CH_3COO)_2·4H_2O$ was added to the above mixture with vigorous stirring. In another beaker, 0.5 mmol of KBr was dissolved in 0.1 M mannitol solution (5 mL) in water. The KBr solution was added dropwise to the $Bi(NO_3)_3·5H_2O$ solution with vigorous stirring (1000 rpm). The reaction mixture was stirred for 30 minutes, and thereafter, the pH was adjusted to 11.5 with the addition of 1.0 M NaOH. The solution was heated at 160 °C for 20 hours in an autoclave and thereafter cooled down to room temperature gradually. The reaction mixture was washed repeatedly with distilled water and ethanol. The off-white color with greenish taint powder compound was isolated by centrifugation and dried at 50 °C overnight. Bi_3O_4Br was prepared following the same protocol without' added nickel salt during the preparation.

Characterization techniques

Crystal structure and phase identification studies were carried out through X-ray diffractometer (XRD, Pananalytical) using a Cu K_α source with wavelength, $\lambda = 1.54$ Å. The Raman scattering measurements were conducted using an electrically cooled CCD camera coupled with an Olympus BX41 Raman spectrometer by WITEC with laser lines at 532 nm. The absorption of light in the wavelength range 300–800 nm was studied by UV-vis diffuse reflectance spectroscopy (DRS) (UV-vis Cary series, Agilent Technologies). A Metrohm Auto lab PGSTAT 204 potentiostat galvanostat was used for all electrochemical measurements with a conventional three-electrode system at room temperature (298 K) using Nova 2.1.6 software. Transmission electron microscopy (TEM) analysis was performed by a Thermo Scientific, Themis 300 G3 instrument. The sample was drop cast on a carbon coated 300 mesh Cu grid (Ted Pella, Inc.) for TEM analysis. Fourier transform infrared spectroscopy (FTIR) (Vertex 70v, Bruker) was performed to understand the bonding structure. XPS was performed with a PHI-5702 X-ray photoelectron spectrometer.

Electrochemical measurements

All the electrochemical studies were performed by using the Metrohm Auto lab potentiostat with a conventional three-electrode system at room temperature (298 K). The pH of the solutions was adjusted using an ORION STAR A111 (Thermo Scientific) or LMPH-9 (Labman Scientific) pH Meter. A spiral platinum electrode (Pt) and an Ag/AgCl electrode submerged in 3.0 M KCl were taken as the counter and reference electrodes, respectively. The catalyst ink was then prepared by taking 3.0 mg of catalyst in the solution of 120 μL of HPLC grade IPA, 80 μL of millipore water (18.2 MΩ cm at 298 K), and 30 μL

of 5 wt% Nafion. The prepared catalyst was deposited on carbon fiber paper (with approximate mass loading of 1.04 mg cm^{-2}) and directly used as the working electrode. 1.0 M KOH solution (pH 14.0) was utilized as the electrolyte solution. Before performing the linear sweep voltammetry (LSV) and electrochemical impedance spectroscopy (EIS), 100 cycles of cyclic voltammetry (CV) were performed with a 50 mV s^{-1} scan rate to obtain a steady state of the electrocatalysts. The Nyquist plots were measured by the application of a sinusoidal wave with an AC amplitude of 10 mV from the 10^5 Hz to 0.1 Hz operating frequency range. The potential values were measured against the Ag/AgCl reference electrode, which was then converted to a reversible hydrogen electrode (RHE) by using this equation.

$$E_{RHE}\ (V) = E_{Ag/AgCl}\ (V) + 0.059pH + E_{applied}$$

where $E_{applied}$ is the applied potential. Hydroxymethyl ferrocene ($E = +0.385$ V at SHE) was added as an internal standard to measure the exact potential of the reference electrode. All the mentioned potentials, in this work are the values concerning RHE.

Results and discussion

The pristine Bi_3O_4Br and Ni-doped Bi_3O_4Br were synthesized *via* the hydrothermal process. The crystalline structures and associated crystal phases of Bi_3O_4Br and Ni-doped Bi_3O_4Br were identified by deploying powder X-ray diffraction (XRD). All the peaks for the Bi_3O_4Br were indexed with the already existing literature that implied the presence of an orthorhombic unit cell (Fig. 1).[29,34] The XRD signals broadened following the Ni-doping, suggesting that the inclusion of Ni in the structure reduces the crystallinity of Bi_3O_4Br. Ni-doping possibly creates bismuth and oxygen vacancies in the matrix due to the size mismatch to induce a change in the crystallinity of Bi_3O_4Br. The influence of the Ni-doping was specifically vivid with a shift

Fig. 1 Powder XRD patterns for the Bi_3O_4Br and Ni-doped Bi_3O_4Br.

observed for the peaks associated with the (112) and (114) planes, while the rest of the peaks remained constant.

The X-ray photoelectron spectroscopic (XPS) study was performed next to further confirm the chemical composition, electronic structure, and valence state of each element present in Bi_3O_4Br and Ni-doped Bi_3O_4Br (Fig. 2). All the XPS spectra were corrected for specimen charging by referencing the C1s peak to 284.60 eV. Two high-intensity peaks in the high-resolution XPS spectra of Bi are observed at 158.48 eV and 163.81 eV that are assigned as Bi 4f$_{7/2}$ and Bi 4f$_{5/2}$, respectively, with a splitting energy Δ = 5.33 eV (Fig. 2a).[35] On the contrary, the Bi 4f$_{7/2}$ and Bi 4f$_{5/2}$ peaks for the Ni-doped Bi_3O_4Br were red-shifted by 0.2 eV compared to the pristine Bi_3O_4Br. This low-energy shift indicates that the electronic environment around the bismuth atom has changed slightly after nickel doping. The two high-intensity peaks denote the +3 oxidation state of Bi in the Bi–O bonding inside the crystal lattice, and the slight shift towards lower binding energy (by 0.2 eV) following the Ni-addition possibly suggests an elongated Bi–O bonding in the Ni-doped Bi_3O_4Br. It is important to mention that the very low-intensity shoulders around 156.2 eV and 161.4 eV are due to the Bi 4f$_{7/2}$ and Bi 4f$_{5/2}$, respectively, arising from the Bi^{3+} sites of the Bi–Br bonding. O 1s showed two peaks with the binding energy values of 529.02 eV and 530.22 eV in Bi_3O_4Br with a splitting energy Δ = 1.2 eV. These two peaks are assigned to oxygen present in the vicinity of oxygen defects and the lattice oxygen (bound to metal, Bi), respectively (Fig. 2b).[35] Similar peaks were observed at slightly higher energies of 529.92 eV and 531.80 eV with a splitting energy Δ = 1.88 eV. Such a shift in binding energy presumably appeared due to the redistribution of the electronic charge around the O atoms subsequent to the Ni-addition. The oxygen defect peak is relatively higher in intensity in the case of Ni-doped Bi_3O_4Br compared to pristine Bi_3O_4Br. Hence, the XPS data insinuates that the Ni-doped Bi_3O_4Br is more defect-rich in terms of oxygen vacancies than the pristine Bi_3O_4Br. Similarly, two Br peaks were observed at 67.6 eV and 68.70 eV and were allocated to Br 3d$_{5/2}$ and Br 3d$_{3/2}$, respectively (Fig. 2c).[30] A Ni 2p$_{3/2}$ peak is observed at 854.88 eV for the Ni-doped sample, which can be assigned to the +2 oxidation state of Ni (Fig. 2d).[36,37] Lastly, the valence band XPS spectra show that the Ni doping shifts the valence band (VB) towards a more (0.05 eV) positive side in the energy scale with higher oxidizing ability than the pristine Bi_3O_4Br. From the XPS peak area analysis, the presence of Ni was observed as *ca* $\sim$ 0.4 atomic %.

A transmission electron microscopy (TEM) study was performed for the morphological investigation of the materials. The TEM images of pure Bi_3O_4Br and Ni-doped Bi_3O_4Br represent the 2D-plate-like morphology (Fig. 3, and Fig. S1, ESI†). The fast Fourier transform (FFT) is used to convert the raw image data obtained from the transmission electron microscope into a frequency domain representation. This permits the analysis of the spatial frequency content of the image, which can provide information about the crystal structure, defects, and other features of the sample being studied. The FFT is particularly useful for analysing diffraction patterns, which can
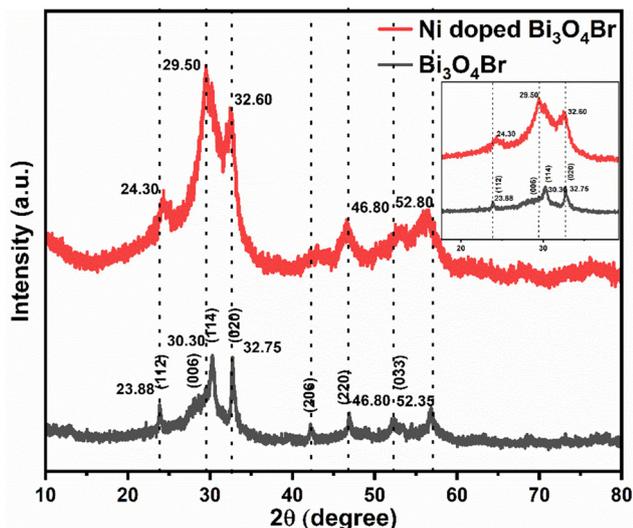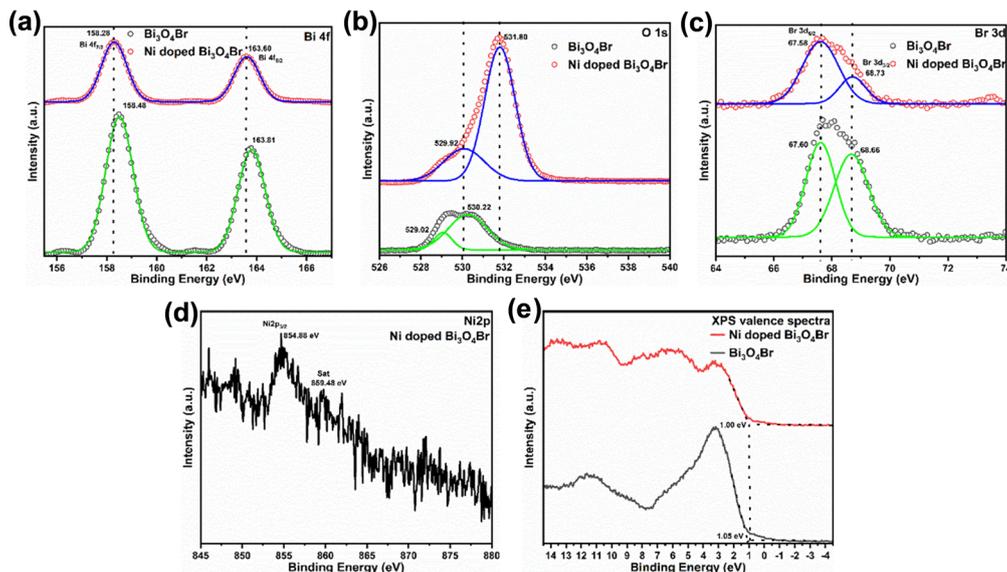
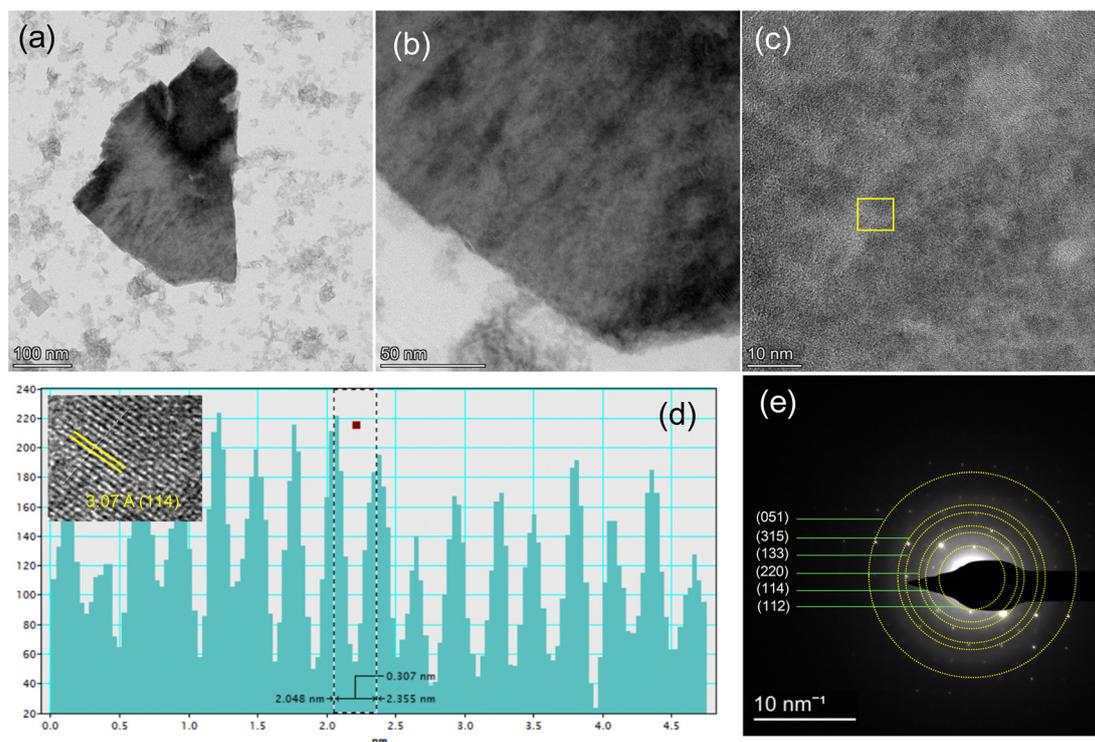Fig. 2   High resolution XPS spectra of (a) Bi 4f, (b) O 1s, (c) Br 3d, (d) Ni 2p, and (e) valence spectra for Bi_3O_4Br and Ni-doped Bi_3O_4Br.

Fig. 3   (a) and (b) TEM images of Ni-doped Bi_3O_4Br, (c) HR-TEM image, and (d) line-scanning intensity profile of the inserted inverse FFT and live FFT of the selected area in (c). (g) SAED pattern of Ni-doped Bi_3O_4Br, (FFT = fast Fourier transition).

provide valuable information about the atomic arrangement within a material. The obtained FFT contains diffraction spots (reciprocal space pattern), which can be further used to create images of the region of interest using the inverse FFT method. HR-TEM image and inverse fast Fourier transition (FFT) analysis confirmed the presence of the (114) plane on the surface of the Ni-doped Bi_3O_4Br nanostructure (Fig. 3c and d). It is worth

mentioning that this (114) plane displayed a distinct shift following the Ni-doping to Bi_3O_4Br. Selected area electron diffraction (SAED) is a crystallographic experimental technique performed using a transmission electron microscope. In the SAED pattern, each obtained spot corresponds to a satisfied diffraction condition. For any crystalline nanomaterial, SAED patterns typically provide an image composed of single spots

(dots) only if it is a single crystal, and a ring pattern for a polycrystalline material. This feature of SAED is useful for distinguishing crystalline nanomaterials from their amorphous counterparts. Herein, the selected area electron diffraction (SAED) pattern of Ni-doped Bi_3O_4Br reveals the formation of a polycrystalline nanostructured material (Fig. 3e). The high-angle annular dark-field scanning transmission electron microscopy image and corresponding elemental mapping confirm the uniform distribution of Bi, O, Br, and Ni elements in the Ni-doped Bi_3O_4Br nanostructures (Fig. 4 and Fig. S2, ESI†). Analogous data was also recorded for pristine Bi_3O_4Br (Fig. S3, ESI†).

The optical absorption properties of Bi_3O_4Br and Ni-doped Bi_3O_4Br were investigated by UV-vis absorption and diffuse reflectance spectra (DRS). A significant optical absorption band for the Ni-doped Bi_3O_4Br was extended beyond 500 nm. However, the analogous band terminates around 450 nm for the Bi_3O_4Br (Fig. S4, ESI†).[31,38,39] This shows that Ni doping shifts the bandgap of Bi_3O_4Br towards the visible region. For crystalline semiconductor materials, the optical absorption near the band edge follows the equation: $\alpha h\nu = A(h\nu - E_g)^{n/2}$, where α, ν, A, and E_g are the absorption coefficient, frequency of light, proportionality constant, and energy bandgap, respectively. The quantity of "n" depends on the characteristics of transition. For a direct bandgap semiconductor, n is taken as 1, and for an indirect bandgap semiconductor, n is taken as 4. Since Bi_3O_4Br is known as an indirect bandgap semiconductor, n is taken as 4. By plotting $(\alpha h\nu)^{1/2}$ *vs.* energy (eV), we have obtained the bandgaps of the Bi_3O_4Br and Ni-doped Bi_3O_4Br as 2.49 eV and 2.36 eV, respectively. From the XPS valence spectra and the diffuse reflectance spectra (DRS), we have obtained the positions of the valence band (VB) and conduction band (CB) in Bi_3O_4Br and Ni-doped Bi_3O_4Br (Fig. 2e and Fig. S4, ESI†). The VB after Ni doping becomes less positive. Hence, the Ni-doped

Bi_3O_4Br is a better oxidizing catalyst than the pristine Bi_3O_4Br. On the other hand, the pristine Bi_3O_4Br is a better reducing catalyst than the Ni-doped Bi_3O_4Br as the position of the CB is more negative for the Bi_3O_4Br than the Ni-doped Bi_3O_4Br.

To further characterize Bi_3O_4Br and Ni-doped Bi_3O_4Br, we also studied Raman and FTIR analysis, as depicted in Fig. S5 (ESI†). The Raman bands centered at 108.9 and 151.34 cm^{-1} belong to the A_{1g} internal and E_g internal Bi–Br stretching modes, respectively (Fig. S5a, ESI†).[39,40] An increased peak intensity and broadening of the signals was observed for Ni-doped Bi_3O_4Br compared to pristine Bi_3O_4Br. This can be attributed to the difference in electron–phonon coupling in the single-unit cell regime for the two compounds. The distinct signatures that appeared in the FTIR spectrum of Bi_3O_4Br at 1450–1190 cm^{-1} can be ascribed to the asymmetric and symmetric stretching vibrations of Bi–Br bonds, while the peak at 524 cm^{-1} is assigned to the Bi–O vibration modes (Fig. S5b, ESI†).[39] A broad band at 3442 cm^{-1} and a peak at 1638 cm^{-1} are associated with the stretching and bending vibration modes of H_2O molecules adsorbed on the surface of Bi_3O_4Br during FTIR analysis.[41] Similar characteristic peaks were also observed in the FTIR spectrum of the Ni-doped Bi_3O_4Br material.

Electrochemical and photoelectrochemical HER performance

The electrocatalytic HER performances of Bi_3O_4Br and Ni-doped Bi_3O_4Br were studied by a series of electrochemical experiments in 1.0 M KOH (pH ~14.0) with a standard three-electrode system. Linear sweep voltammetry (LSV) measurements showed that Ni-doped Bi_3O_4Br exhibited an overpotential of 545 and 662 mV to achieve a conventional current density of 10 and 50 mA cm^{-2}, respectively. On the other hand, pristine Bi_3O_4Br showed an overpotential of 547 and 736 mV to attain the same current density (Fig. 5a). Hence, there is a significant
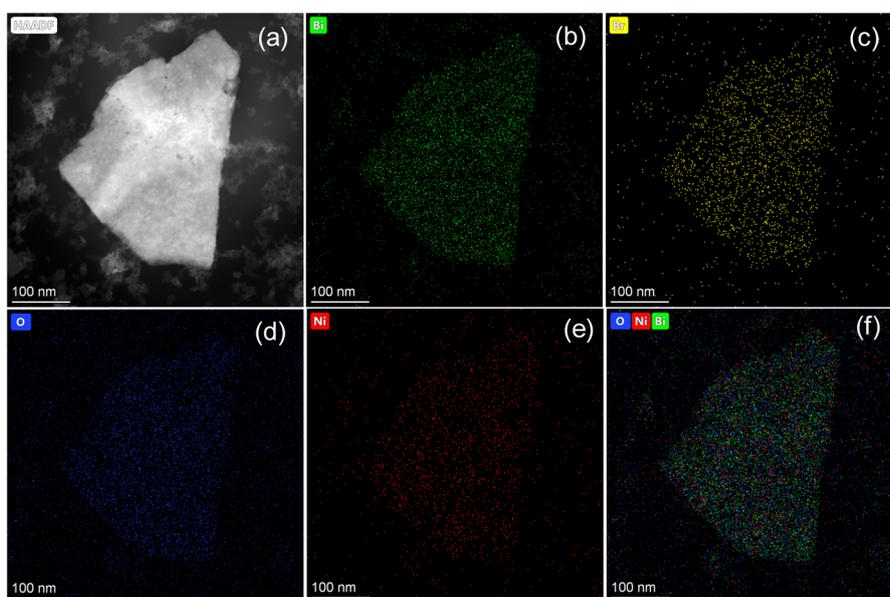

Fig. 4 (a) HAADF image of Ni-doped Bi_3O_4Br for the elemental mapping of (b) Bi, (c) Br, (d) O, (e) Ni, and (f) mixed elements of Bi, O, and Ni.
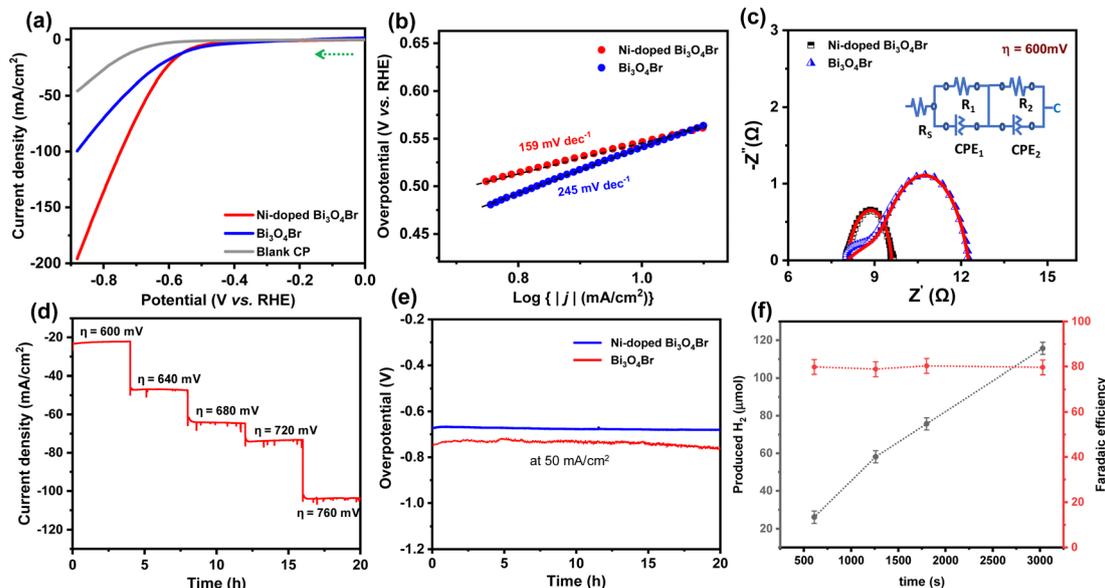
Fig. 5 (a) LSV polarization curves, (b) corresponding Tafel plots, (c) electrochemical impedance spectra obtained at an overpotential of 600 mV of the Ni-doped Bi_3O_4Br and Bi_3O_4Br catalysts. (d) Potential dependent chronoamperometry stability test of Ni-doped Bi_3O_4Br, (e) chronopotentiometry stability of Ni-doped Bi_3O_4Br and Bi_3O_4Br. (f) Time dependent hydrogen gas production (μmol) and faradaic efficiency of the Ni-doped Bi_3O_4Br catalyst during chronoamperometry study at −0.6 V vs. RHE.

deterioration in overpotential at higher current density after the Ni-doping into Bi_3O_4Br. The reaction kinetics of the catalysts were examined by Tafel slope analysis of the catalysts (Fig. 5b). A relatively low Tafel slope of 159 mV dec^{-1} was exhibited by Ni-doped Bi_3O_4Br compared to the pristine Bi_3O_4Br (245 mV dec^{-1}), which indicated a better HER kinetics for the Ni-doped sample in an alkaline medium. Electrochemical impedance spectroscopy (EIS) was carried out at an applied overpotential of 600 mV to have a better insight into the charge transfer resistance (R_{ct}) at the electrode and electrolyte interface. The obtained EIS spectra and corresponding circuit diagrams are represented in Fig. 5c, where R_s is the resistance of the electrolyte, and CPE is a constant phase element. The lower R_{ct} value of Ni-doped Bi_3O_4Br (1.55 Ω) further confirms higher electron transfer ability across the electrode and electrolyte interface than that of Bi_3O_4Br (5.12 Ω) during the HER process. Therefore, it can be concluded that Ni-doping substantially improves the background HER activity of Bi_3O_4Br.

To explore the enhanced activity, double layer capacitance (C_{dl}) values of the catalysts were measured, followed by the electrochemically active surface area (ECSA) from CV measurements in a non-faradaic potential region (Fig. S6, ESI†). A higher ECSA value (40.5 cm^2) was observed for the Ni-doped Bi_3O_4Br catalyst in comparison to the precursor Bi_3O_4Br (31.5 cm^2). This data implies that Ni-doped Bi_3O_4Br possesses more active sites, which is beneficial for the adsorption of water molecules and close contact with the electrolyte during HER catalysis. The LSV results of the materials are normalized with these obtained electrochemically active surface area values to provide the intrinsic effect of Ni-doping in the Bi_3O_4Br template (Fig. S7, ESI†). The ECSA normalized LSV plots represent that the HER activity trend is maintained, as it is in the geometric area normalized polarization curve for Ni-doped Bi_3O_4Br and

Bi_3O_4Br catalysts. Moreover, the mass activity of Bi_3O_4Br was improved drastically from 52 to 98 A g^{-1} after incorporation of Ni in the pristine nanostructure (Fig. S8, ESI†).

In addition to showcasing the HER performance, long-term stability is another crucial factor for a promising electrocatalyst that can be translated to industrial applications. A potential-dependent chronoamperometry stability test was performed with 4.0 hour intervals (Fig. 5d). The chronoamperometry stability test demonstrated consistent current densities at different applied overpotential values. In addition, we have studied the chronopotentiometry stability of the Ni-doped Bi_3O_4Br and Bi_3O_4Br catalysts at the current density of 50 mA cm^{-2} which exhibited an enhancement in the overpotential of 13 and 17 mV after 20 hours, respectively (Fig. 5e). Therefore, Ni-doped Bi_3O_4Br demonstrates superior durability in a strongly alkaline medium while displaying HER activity. Interestingly, the pristine Bi_3O_4Br catalyst exhibited a significant loss of 19% current density after an analogous 20 hours chronoamperometry stability test (Fig. S9, ESI†). Notably, the incorporation of Ni ions into Bi_3O_4Br not only enhanced the HER activity but also improved the durability of the catalyst. Faradaic efficiency is an important parameter to measure the efficiency of charge transfer in an electrochemical reaction. It was measured by comparing the theoretically and experimentally obtained amount of H_2, which was evaluated using a gas chromatography (GC) instrument equipped with a TCD detector and 5 Å molecular sieve column for separation of the gases with argon as the carrier gas (CIC Dhruva). The GC instrument was calibrated using three standard gas samples containing 1%, 2%, and 5% H_2, respectively. The Bi_3O_4Br and Ni-doped Bi_3O_4Br catalyst exhibited a faradaic efficiency of ~65 and 79% for the HER in an alkaline medium (pH ~14.0) with constant

growth in accumulated H_2 during the chronoamperometric experiment (Fig. 5f and Fig. S10 and S11, ESI†).

Moreover, we have also studied the photoelectrochemical HER performance under UV-vis light irradiation. LSV measurements displayed that Bi_3O_4Br exhibited an overpotential of 614 and 668 mV to achieve a conventional current density of 10 and 50 mA cm^{-2}, whereas the same current density was exhibited by Ni-doped Bi_3O_4Br at the overpotential of 418 and 614 mV, respectively (Fig. 6a). Therefore, a significant improvement in overpotential was observed in the HER performance under UV-vis light irradiation. Furthermore, a substantial increase in photocurrent response by 60% was observed for the Ni-doped Bi_3O_4Br compared to that of Bi_3O_4Br in the PEC measurements, indicating that enhanced charge separation occurred due to the incorporation of Ni in the Bi_3O_4Br catalyst (Fig. 6c and d). The faradaic efficiency of Ni-doped Bi_3O_4Br was calculated to be 87% during the photoelectrocatalytic HER, which was ∼33% and 10% superior to that of Bi_3O_4Br, and Ni-doped Bi_3O_4Br during the electrocatalytic HER process, respectively (Fig. 6b and Fig. S11, ESI†).

We have studied the post-electrocatalytic ECSA of the Ni-doped Bi_3O_4Br catalyst, which was found to be 1.51 cm^2 (Fig. S14, ESI†). The 6.79% decrease in electrochemically active surface area may be due to the leaching out of Ni, which is one of the effective active areas. This statement can also be supported by the before and post-catalytic ICP-AES analysis of the Ni-doped Bi_3O_4Br catalyst as described in the ESI.† Moreover, we have deeply focused on the stability of the catalyst after the long-term electrochemical HER performance test. The structural stability studied was determined using a powder XRD pattern (Fig. S15, ESI†); on the other hand the morphological stability of the catalyst was investigated by TEM and bright field elemental mapping (Fig. S16 and S17, ESI†). No such morphological and structural deformation was observed after the long-term electrocatalytic HER performance test of the catalyst.

Conclusions

This specific cation doping approach is certainly one of the best ways to explicitly enhance the electrocatalytic HER performance under alkaline conditions with highly exposed active sites. The doping of Ni ions in Bi_3O_4Br facilitated the reduction of the overpotential and improved the kinetics during the HER activity. The electrochemically active surface area and mass activity of Bi_3O_4Br were improved drastically by 29% and 88%,
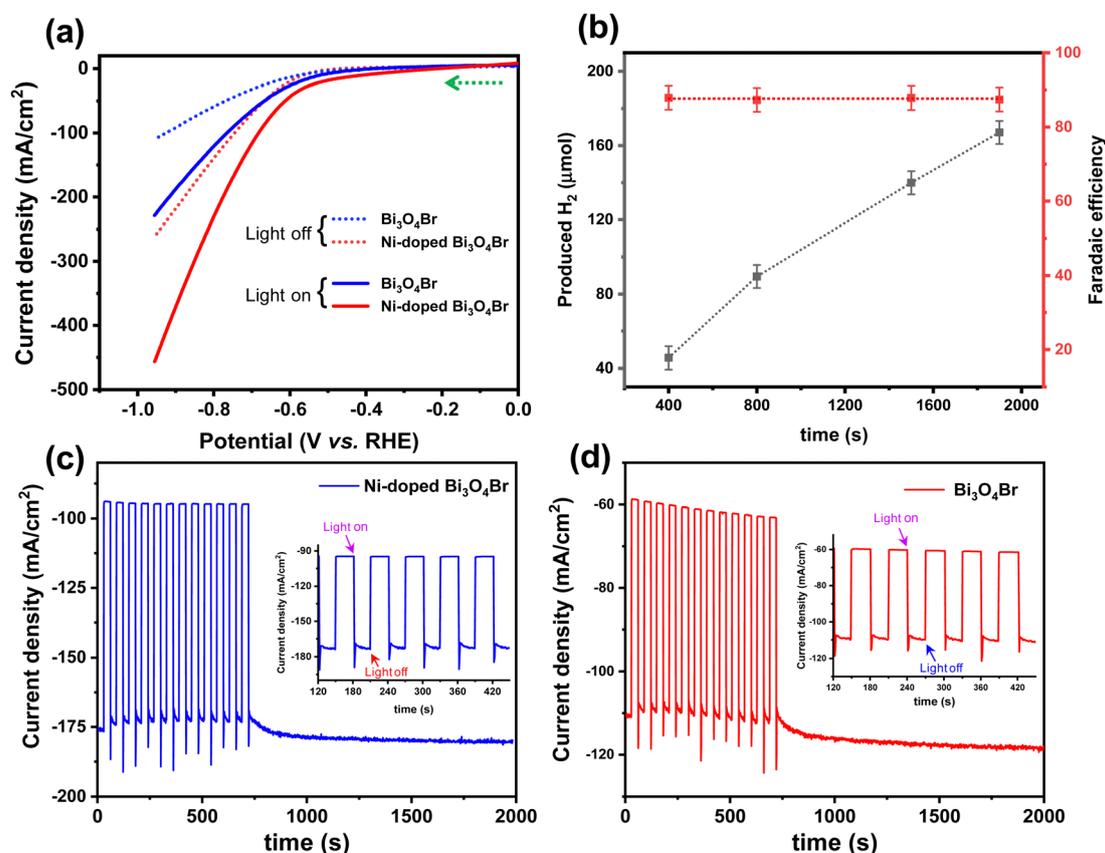

Fig. 6 Photoelectrochemical performance: (a) LSV polarization curves of Ni-doped Bi_3O_4Br and Bi_3O_4Br catalysts in the presence and absence of light, (b) amount of H_2 produced and faradaic efficiency of Ni-doped Bi_3O_4Br during chronoamperometry study at −0.62 V vs. RHE. (c) and (d) Photocurrent response (in chopping mode, light on−off repeatedly) of the Ni-doped Bi_3O_4Br and Bi_3O_4Br catalysts under UV-vis light irradiation (300 W Xe lamp) at an applied potential of −0.73 V (vs. RHE) in 1 M KOH solution.

respectively, after the incorporation of Ni ions in the pristine nanostructure. Substantial improvement in the HER performance and faradaic efficiency were also observed under UV-vis light irradiation that contributes to the accelerated evolution of hydrogen in the photocatalysis system. The durability of the Bi_3O_4Br template was also enhanced following the Ni-doping, which was evident from the stable current density and negligible change in overpotential during a 20-hour stability test at an applied current density of 50 mA cm^{-2}. The present work not only demonstrates a facile approach to fabricate cost-effective HER catalysts but also explores a new route to develop a sustainable and highly efficient robust electrocatalyst derived from the family of transition metal-doped semiconductor materials. Ni-doped Bi_3O_4Br nanostructured materials can further be used in the field of sensors, supercapacitors, and photochemical small molecule activation reactions, aiding the journey towards a carbon-neutral landscape.

Author contributions

SB and AD conceptualized the project; MP, RB, and SB performed the experiments; MP, RB, SB, and AD analyzed the data; RB, SB and AD wrote the manuscript; SB and AD revised and edited the manuscript; AD supervised the project.

Conflicts of interest

The authors declare no competing financial interest.

Acknowledgements

References

1 S. Chu, Y. Cui and N. Liu, *Nat. Mater.*, 2017, **16**, 16–22.
2 I. A. Liyanage, H. Barmore and E. G. Gillan, *Energy Adv.*, 2023, **2**, 1831–1842.
3 M. N. I. Salehmin, T. Husaini, J. Goh and A. B. Sulong, *Energy Convers. Manage.*, 2022, **268**, 115985.
4 G. Srividhya, C. Viswanathan and N. Ponpandian, *Energy Adv.*, 2023, **2**, 1464–1475.
5 H. Lin, Z. Shi, S. He, X. Yu, S. Wang, Q. Gao and Y. Tang, *Chem. Sci.*, 2016, **7**, 3399–3405.
6 Z. Chen, W. Gong, S. Cong, Z. Wang, G. Song, T. Pan, X. Tang, J. Chen, W. Lu and Z. Zhao, *Nano Energy*, 2020, **68**, 104335.
7 B. H. Honnappa, S. Mohan, M. Shanmugam, A. Augustin, P. J. Sagayaraj, C. Chuaicham, S. Rajendran, T. K. A. Hoang, K. Sasaki and K. Sekar, *Energy Adv.*, 2022, **1**, 738–760.
8 S. Das, C. Das, N. A. Shah, S. Ghorai, P. Majumder and A. Dutta, *Chem. Commun.*, 2023, **59**, 7243–7246.
9 R. T. Parayil, S. K. Gupta, M. Pal, A. Dutta, D. Tyagi, K. Sudarshan and M. Mohapatra, *RSC Adv.*, 2023, **13**, 31101–31111.
10 S. Mansingh, K. K. Das and K. Parida, *Sustainable Energy Fuels*, 2021, **5**, 1952–1987.
11 R. Biswas, I. Ahmed, P. Manna, P. Mahata, R. S. Dhayal, A. Singh, J. Lahtinen and K. K. Haldar, *ChemPlusChem*, 2023, **88**, e202200320.
12 A. P. Murthy, J. Madhavan and K. Murugan, *J. Power Sources*, 2018, **398**, 9–26.
13 W. Yang and S. Chen, *Chem. Eng. J.*, 2020, **393**, 124726.
14 K. Zhang and R. Zou, *Small*, 2021, **17**, 2100129.
15 A. Banerjee, M. K. Awasthi, P. Maji, M. Pal, S. T. Aziz, G. K. Lahiri and A. Dutta, *ChemElectroChem*, 2023, **10**, e202201098.
16 R. Biswas, P. Thakur, G. Kaur, S. Som, M. Saha, V. Jhajhria, H. Singh, I. Ahmed, B. Banerjee and D. Chopra, *Inorg. Chem.*, 2021, **60**, 12355–12366.
17 J. S. Kim, B. Kim, H. Kim and K. Kang, *Adv. Energy Mater.*, 2018, **8**, 1702774.
18 S. T. Aziz, M. Ummekar, I. Karajagi, S. Riyajuddin, K. Siddhartha, A. Saini, A. Potbhare, R. G. Chaudhary, V. Vishal and P. C. Ghosh, *Cell Rep. Phys. Sci.*, 2022, **3**, 101106.
19 K. S. Sairam, S. T. Aziz, I. Karajagi, A. Saini, M. Pal, P. C. Ghosh and A. Dutta, *Int. J. Hydrogen Energy*, 2023, **48**, 10521–10531.
20 J. Yu, T. A. Le, N. Q. Tran and H. Lee, *Chem. – Eur. J.*, 2020, **26**, 6423–6436.
21 J. Mohammed-Ibrahim and X. Sun, *J. Energy Chem.*, 2019, **34**, 111–160.
22 V. Pundir, A. Gaur, R. Kaur and V. Bagchi, *Energy Adv.*, 2023, **2**, 321–327.
23 V. Manjunath, S. Bimli, R. Biswas, P. N. Didwal, K. K. Haldar, M. Mahajan, N. G. Deshpande, P. A. Bhobe and R. S. Devan, *Int. J. Hydrogen Energy*, 2022, **47**, 39018–39029.
24 R. Biswas, A. Kundu, M. Saha, V. Kaur, B. Banerjee, R. S. Dhayal, R. A. Patil, Y.-R. Ma, T. Sen and K. K. Haldar, *New J. Chem.*, 2020, **44**, 12256–12265.
25 J. Ran, J. Zhang, J. Yu, M. Jaroniec and S. Z. Qiao, *Chem. Soc. Rev.*, 2014, **43**, 7787–7812.
26 X. Wei, M. U. Akbar, A. Raza and G. Li, *Nanoscale Adv.*, 2021, **3**, 3353–3372.
27 J. Di, J. Xia, H. Li, S. Guo and S. Dai, *Nano Energy*, 2017, **41**, 172–192.
28 J. Xiong, P. Song, J. Di and H. Li, *J. Mater. Chem. A*, 2020, **8**, 21434–21454.
29 J. Di, C. Chen, S.-Z. Yang, S. Chen, M. Duan, J. Xiong, C. Zhu, R. Long, W. Hao and Z. Chi, *Nat. Commun.*, 2019, **10**, 2840.
30 F. Zhang, X. Xiao and Y. Xiao, *J. Alloys Compd.*, 2022, **923**, 166417.
31 J. Wang, Y. Yu and L. Zhang, *Appl. Catal., B*, 2013, **136**, 112–121.

32 X. Jiang, X. He, H. Huang, Y. Li, J. Yang, J. Mei and S. Cui, *J. Alloys Compd.*, 2023, **963**, 171221.

33 X. Wang, Z. Wang, Y. Li, J. Wang and G. Zhang, *Appl. Catal., B*, 2022, **319**, 121895.

34 Y. Zhang, F. Guo, K. Wang, J. Di, B. Min, H. Zhu, H. Chen, Y.-X. Weng, J. Dai and Y. She, *Chem. Eng. J.*, 2023, **465**, 142663.

35 J. Hu, F. Chen, K. Mu, J. Zhang and J. Lu, *Sep. Purif. Technol.*, 2022, **286**, 120416.

36 R. Biswas, P. Thakur, I. Ahmed, T. Rom, M. S. Ali, R. A. Patil, B. Kumar, S. Som, D. Chopra and A. K. Paul, *Energy Fuels*, 2022, **37**, 604–613.

37 I. Ahmed, R. Biswas, S. G. Dastider, H. Singh, S. Mete, R. A. Patil, M. Saha, A. K. Yadav, S. N. Jha and K. Mondal, *Energy Fuels*, 2022, **36**, 12160–12169.

38 K.-L. Li, W. W. Lee, C.-S. Lu, Y.-M. Dai, S.-Y. Chou, H.-L. Chen, H.-P. Lin and C.-C. Chen, *J. Taiwan Inst. Chem. Eng.*, 2014, **45**, 2688–2697.

39 R. Li, J. Feng, X. Zhang, F. Xie, J. Liu, C. Zhang, Y. Wang, X. Yue and C. Fan, *Sep. Purif. Technol.*, 2020, **247**, 117007.

40 A.-H. Lee, Y.-C. Wang and C.-C. Chen, *J. Colloid Interface Sci.*, 2019, **533**, 319–332.

41 R. Biswas, S. Mete, M. Mandal, B. Banerjee, H. Singh, I. Ahmed and K. K. Haldar, *J. Phys. Chem. C*, 2020, **124**, 3373–3388.